Batteries & Supercaps

Research Article
doi.org/10.1002/batt.202200222

Chemistry Europe
European Chemical
Societies Publishing

www.batteries-supercaps.org

Conformal Lithium Peroxide Growth Kinetically Driven by MoS$_2$/MoN Heterostructures Towards High-Performance Li—O$_2$ Batteries

Yuting Gu,[a] Yong Ma,[a] Le Wei,[a] Yuebin Lian,[a, b] Ying He,[a] Yanhui Su,[a] Xinjian Li,[a] Yang Peng,[a] and Zhao Deng*[a]

The morphological control and spatial accommodation of Li$_2$O$_2$ discharge products on the oxygen cathode are crucial to bolstering both the Coulombic and round-trip efficiencies of Li—O$_2$ batteries. Herein, MoS$_2$/MoN heterostructures are constructed on carbon cloth to serve as the freestanding and binder-free oxygen cathode for Li—O$_2$ batteries, lending a low charge/discharge polarization of 0.79 V, a large specific capacity of 9.04 mAh cm^{-2}, and a superb cycling stability beyond 800 h. Through comprehensive microscopic, electroanalytical and density function theory analyses, the superb electrochemical performance is attributed to the formation of a conformal and amorphous Li$_2$O$_2$ layer, which is kinetically driven in virtue of the higher electric conductivity of MoN and stronger LiO$_2$ intermediate adsorption on the heterostructures. This work advocates the merits of interfacial engineering to enhance the performance of Li—O$_2$ batteries by manipulating the discharge product formation.

Introduction

The aprotic Li—O$_2$ battery with a theoretical energy density of ~3500 Wh kg^{-1} has been reckoned as one of the next-gen energy storage solutions to surmount the current limit of lithium-ion technologies.[1–3] Based on the overall triphasic reaction of $2Li^+ + O_2 + 2e^- \leftrightarrow Li_2O_2$ ($E° = 2.96$ V vs. Li/Li$^+$), the reversibility and kinetics of the electrochemical process are closely related to the mass transport of Li$^+$ and O$_2$, the conduction and redox transfer of electrons, as well as the spatial accommodation of insulative Li$_2$O$_2$ on the air cathode, where a bifunctional ORR/OER catalyst is typically loaded to lower the charge/discharge overpotential and enhance the Coulombic efficiency.[4–6] Particularly, the morphology and distribution of Li$_2$O$_2$ induced via different reaction cascade during ORR play a pivotal role in balancing the battery capacity and round-trip energy efficiency.[7–9] For instance, toroidal Li$_2$O$_2$ products that are typically resulted from the "solvation-mediated growth" mechanism contribute to larger discharge capacity but at the cost of high charge overpotential, due to their poor contact with the catalytic sites and the sluggish mass and charge kinetics in bulk crystals.[10–12] On the other hand, amorphous Li$_2$O$_2$ in the format of thin film or grainy

domains yielded through the "surface-growth" mechanism are easier to decompose during OER in virtue of the more intimate contact with the catalytic scaffold, leading to enhanced charge/discharge kinetics and reversibility.[13–15] However, excessive accumulation of the insulating Li$_2$O$_2$ would soon mask the active sites and blockade the charge conduction path, reducing not only the battery capacity, but also the cycling life. Therefore, it is imperative to search for suitable material chemistry and architecture to endow high charge transitivity, catalytic activity, and discharge product accommodation for solving such dilemma of capacity and efficiency.

2D transition metal dichalcogenides, such as MoS$_2$, MoSe$_2$, and CoSe$_2$, have been regarded as the potent electrocatalysts to catalyze reversible oxygen conversion.[16–20] However, their semi-conductive nature with a relatively wide band gap significantly impedes the charge conduction (despite the notable catalytic activity), and thereby limits their applications as the oxygen cathode catalysts in Li—O$_2$ batteries. To overcome this limit, heterostructure construction by coupling two different functional moieties through interfacial engineering has been proposed as an effective strategy.[21–23] In this vein, a diversity of heterostructures comprising NiS$_2$/ZnIn$_2$S$_4$, TiO$_2$-Fe$_2$O$_3$, and NiCo$_2$S$_4$@NiO etc. have been introduced and shown to work well in catalyzing the reversible formation/decomposition of Li$_2$O$_2$ in Li—O$_2$ batteries, improving both the Coulombic and round-trip efficiencies.[11,24,25] Nonetheless, the majority of previous studies on heterostructures have been concerned with the electronic-structure modulated OER/ORR behaviors, with less attention paid to their structural effect on tailoring the LiO$_2$ intermediate energetics, which is indeed the crucial descriptor to navigate the "solvation-mediated" and "surface-growth" pathways.[26–28] Consequently, one key aspect of heterostructure construction would be to find a suitable

chemistry to modulate the LiO_2 adsorption behavior, while simultaneously enhancing the charge transport kinetics.

Based on the above considerations, in the current study we have developed a facile method to construct MoS_2/MoN heterostructures on carbon cloth by sequentially carrying out hydrothermal and nitridation reactions. The in-situ transformation of partial MoS_2 into MoN allows for synergistically enhancing the electronic conductivity, modulating the morphology of discharge products, and leveraging the electronic structure of the catalytic ensemble. As a result, the freestanding oxygen cathode with heterostructured MoS_2/MoN motifs delivered a large specific capacity of 9.04 mAh cm^{-2} and superb cycling stability extended to 208 cycles (832 h). This work underscores the modulation of Li_2O_2 formation pathway and charge kinetics through interfacial engineering and intermediate tailoring to raise the performance bar of Li–O$_2$ batteries.

Results and Discussion

The synthesis of MoS_2/MoN heterostructures on carbon cloth, denoted as $MoS_2/MoN@CC$, is schematically illustrated in Figure 1(a). Firstly, a uniform MoS_2 layer was grown onto the carbon cloth ($MoS_2@CC$) through the hydrothermal process, exhibiting the entangled petal morphology as shown by the scanning electron microscopy (SEM) images in Figures 1(b) and S1(a). Next, $MoS_2@CC$ was nitridized in the ammonia atmosphere for 1 h to partially convert MoS_2 into MoN, resulting in the heterostructured $MoS_2/MoN@CC$ composite. SEM images show the initial petal morphology of MoS_2 was partly demolished, lending a coarser morphology with less crowded petals (Figures 1c and S1b). By further extending the nitridation time to 4 h, the petal morphology of MoS_2 was mostly lost and replaced by conglomerated particles (Figures 1d and S1c). This sample is denoted as MoN@CC since the X-ray diffraction (XRD)
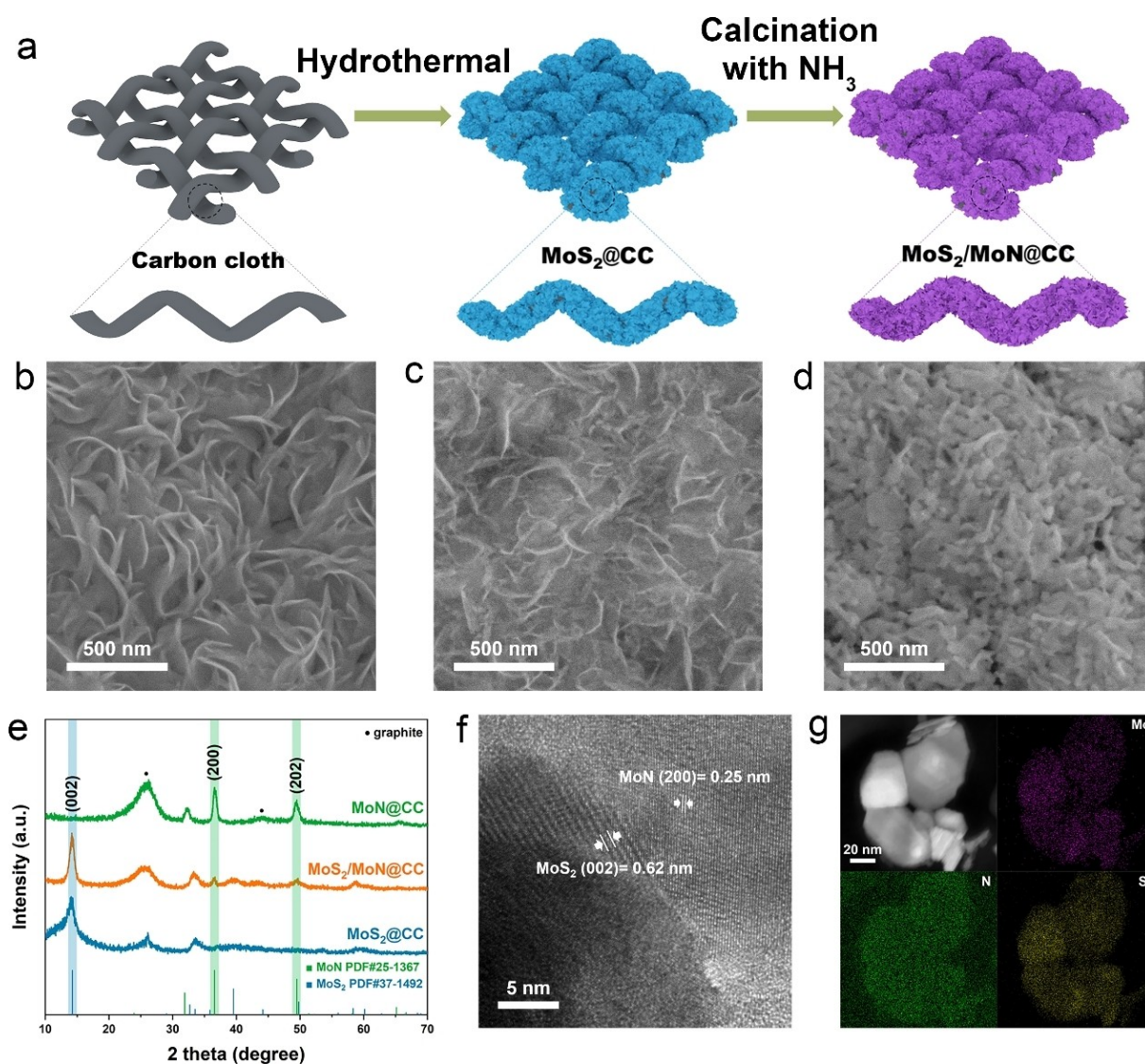
**Figure 1.** Fabrication and structural characterization of $MoS_2/MoN@CC$. a) Schematic illustration of the fabrication of $MoS_2/MoN@CC$. b–d) SEM images of (b) $MoS_2@CC$, (c) $MoS_2/MoN@CC$, and (d) MoN@CC. e) XRD patterns of $MoS_2@CC$, $MoS_2/MoN@CC$, and MoN@CC. f) HR-TEM image exemplifying the heterostructure interface on $MoS_2/MoN@CC$. g) EDX-mapping images of Mo, S and N on $MoS_2/MoN@CC$.

pattern only revealed diffraction peaks that are specific to the (200) and (202) planes of MoN (JCPDS 25-1367, Figure 1e).[29] By contrast, the sample of MoS₂@CC exhibited a prominent peak at 14.2°, corresponding to the (002) plane of 2H-MoS₂ (JCPDS 37-1492),[30] which was not observed on MoN@CC. In addition, Raman spectra further identified the as-prepared MoS₂ turned out to be 2H phase with peaks of in-plane Mo—S phonon mode, out-of-plane Mo—S mode and second-order Raman scattering detected (Figure S2).[31] As a strong evidence for the heterostructure, the XRD pattern of MoS₂/MoN@CC unveiled all the above-mentioned peaks characteristic to both MoS₂ and MoN.

The formation of MoS₂/MoN heterostructures was further confirmed by high-resolution transmission electron microscopy (HR-TEM). Figure 1(f) exemplifies a grain boundary between the MoS₂(002) and MoN(200) planes, in which the (002) plane of MoS₂ displays a large lattice fringe of 0.62 nm and the (200) plane of MoN shows a closely packed lattice of 0.25 nm in d-spacing.[29] At a lower magnification, as shown in Figure 1(g), energy-dispersive X-ray (EDX) mapping images taken under the high angle annular dark field – scanning transmission electron microscopy (HAADF-STEM) mode showed the co-distribution of Mo, N and S elements on MoS₂/MoN@CC, corroborating the coexistence of MoS₂ and MoN.

XPS was used to probe the surface elemental composition and valence states of MoS₂/MoN@CC. The survey spectrum in Figure 2a confirms the heterostructure is composed of Mo, N and S. In the high-resolution Mo 3d spectrum (Figure 2b), three cationic species of Mo can be identified due to multiple valence states, including one doublet at 229.2 and 232.13 eV respectively attributed to the $3d_{5/2}$ and $3d_{3/2}$ spin-orbital states of Mo^{3+} in MoN,[32] one doublet at 229.85 and 232.97 eV ascribed respectively to the $3d_{5/2}$ and $3d_{3/2}$ states of Mo^{4+} in 2H-MoS₂,[33] and one doublet at 233.9 and 236.13 eV assigned to the high-oxidation-state of Mo^{6+} in MoO₃ due to the surface oxidation.[34] Note that the S 2s peak of S^{2-} at 226.99 eV is also adjacent to the Mo 3d signals.[35] Figure 2(c) displays the high resolution N 1s spectrum. It is worth noting that the N 1s signal at 397.78 eV from Mo—N bonding is overlapped with three other Mo $3p_{3/2}$ peaks, designated to Mo—N, Mo—S and Mo—O at 394.9, 395.79 and 399.44 eV, respectively.[36] Lastly, the spectrum of S 2p only points to one S^{2-} state, with its $2p_{3/2}$ and $2p_{1/2}$ spin orbitals located at 162.62 and 163.83 eV, respectively (Figure 2d).[29] Collectively, all the above microscopic and spectroscopic characterizations unequivocally attest to the successful fabrication of MoS₂/MoN heterostructures on carbon cloth through the partial nitridation of MoS₂.

By assembling Li–O₂ batteries, the electrochemical properties of MoS₂/MoN@CC as the freestanding oxygen cathode
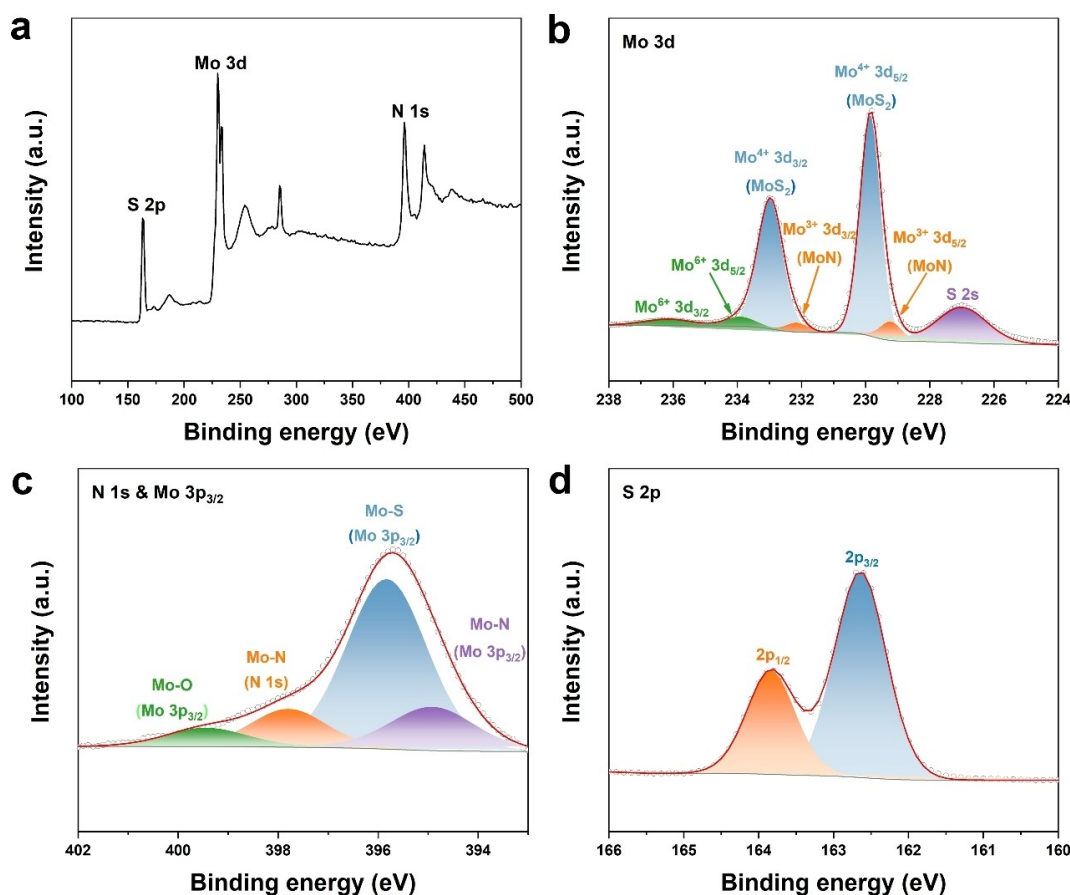
Figure 2. XPS spectra of a) survey, b) Mo 3d and S 2s, c) N 1s and Mo $3p_{3/2}$, and d) S 2p for MoS₂/MoN@CC.

were evaluated and compared to those of MoS$_2$@CC and MoN@CC. Cyclic voltammetry analysis revealed that among the three cathodes, MoS$_2$/MoN@CC had the most positive ORR and negative OER onset potentials, as well as significantly higher current densities (Figure 3a). Notably, both the cathodic and anodic peaks of MoN@CC were nearly negligible, implying that MoN is catalytically inactive, but can help to boost the OER and ORR kinetics of MoS$_2$ by forming the MoS$_2$/MoN heterostructure. As a result, MoS$_2$/MoN@CC displayed the lowest mid-term discharge and charge overpotentials of 0.24 and 0.55 V in the first-cycle discharge/charge profile (acquired at the current density of 0.1 mA cm^{-2} with a cut-off capacity of 0.2 mAh cm^{-2}), accounting for a total polarization of 0.79 V (Figure 3b). In comparison, the mid-term discharge/charge voltage gaps of MoS$_2$@CC and MoN@CC were 1.18 and 1.21 V, respectively. It is worth noting that both the charging curves of the latter two cathodes comprised a staircase, implying a different mecha-

nism of Li$_2$O$_2$ decomposition, which will be discussed later in more details.

When fully discharged at 0.1 mA cm^{-2}, the Li–O$_2$ battery of MoN@CC exhibited a marginal specific capacity of only 0.86 mAh cm^{-2}, whereas that of MoS$_2$/MoN@CC demonstrated a remarkable discharge capacity of 9.04 mAh cm^{-2}, more than double of that for MoS$_2$@CC with a specific capacity of 4.37 mAh cm^{-2} (Figure 3c). Even at a higher current density of 0.2 mA cm^{-2}, MoS$_2$/MoN@CC can still deliver an appreciable discharge capacity of 6.35 mAh cm^{-2}, which is 4 and 40 folds of those obtained by MoS$_2$@CC and MoN@CC, respectively (Figure S3). MoS$_2$/MoN@CC also demonstrated significantly higher rate capability than MoS$_2$@CC and MoN@CC. With the operating current density ramped up from 0.02 to 0.2 mA cm^{-2} and back to 0.02 mA cm^{-2} under a fixed cycling capacity of 0.2 mAh cm^{-2}, MoS$_2$/MoN@CC consistently maintained the lowest charge and discharge overpotentials during the entire
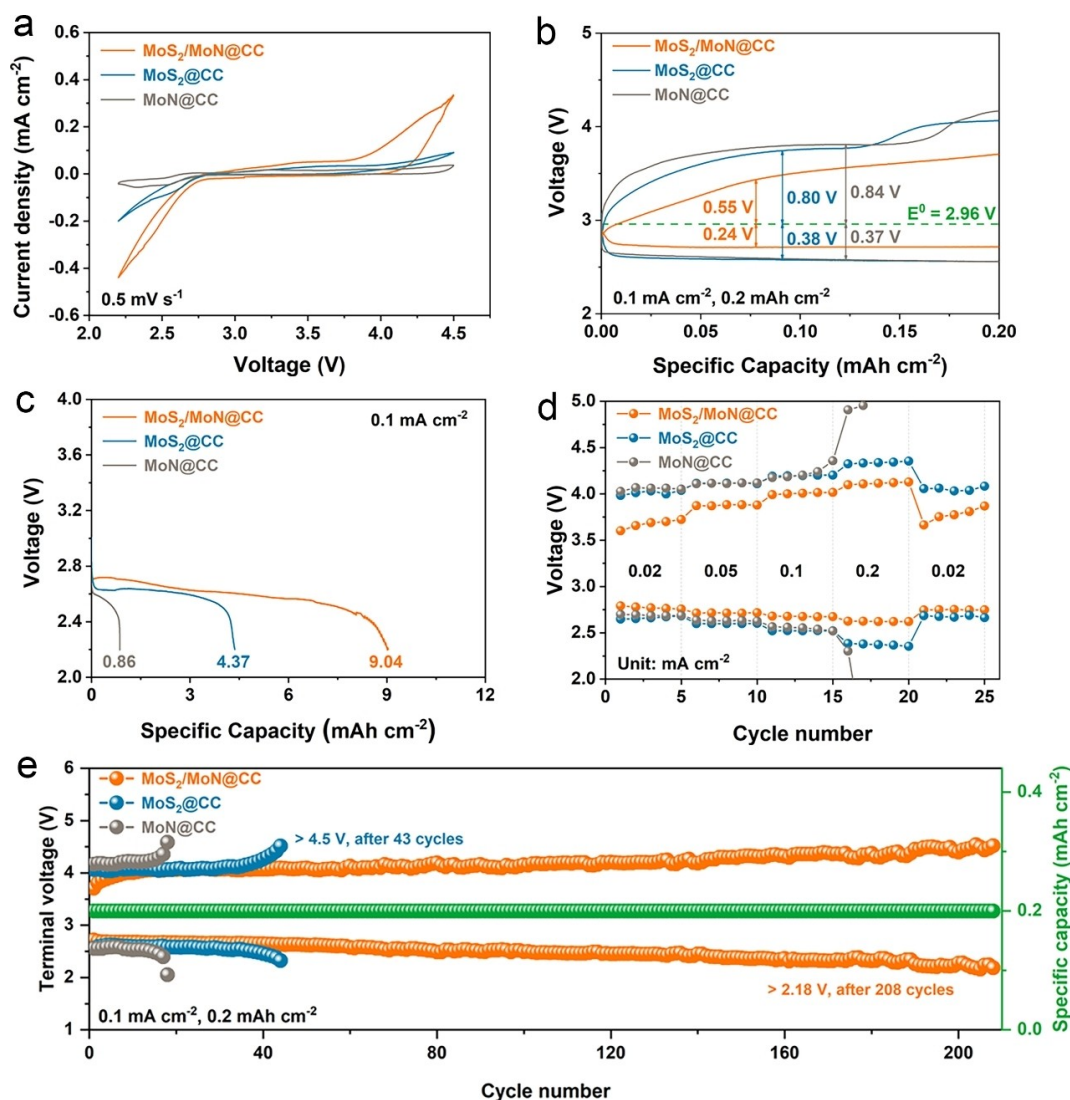
Figure 3. Electrochemical properties of MoS$_2$/MoN@CC, MoS$_2$@CC, and MoN@CC in Li–O$_2$ batteries. a) CV curves taken between 2.2 and 4.5 V at a scan rate of 0.5 mV s^{-1}. b) First-cycle discharge/charge curves at 0.1 mA cm^{-2} with a cut-off capacity of 0.2 mAh cm^{-2}. c) Comparison of total discharge capacities at 0.1 mA cm^{-2}. d) Rate performance at different current densities. e) Plots of discharge and charge terminal voltages vs. cycle number at 0.1 mA cm^{-2} with a cut-off capacity of 0.2 mAh cm^{-2}.

Batteries & Supercaps

Research Article
doi.org/10.1002/batt.202200222

Chemistry Europe
European Chemical
Societies Publishing

galvanostatic test (Figure 3d). Note that at 0.2 mAcm^{-2} the Li–O$_2$ battery of MoN@CC was no longer operational with the charge/discharge voltage gap surpassing 2.6 V. This, again, can be attributed to the poor ORR and OER activities of MoN.

The long-term cycling stability of all three oxygen cathodes were tested with two discharge capacities. At the cycling current density of 0.1 mAcm^{-2} with a fixed cut-off capacity of 0.2 mAhcm^{-2}, the Li–O$_2$ battery of MoS$_2$/MoN@CC was able to continuously operate for 208 cycles (>800 h) until the charging voltage exceeded 4.5 V (Figures 3e and S4a). In a stark contrast, under the same testing conditions the oxygen cathodes of MoS$_2$@CC and MoN@CC can only afford 44 and 18 cycles before the charging voltage hit 4.5 V (Figure S4b and c). With the cycling capacity increased to 0.5 mAhcm^{-2} through more thorough discharging and charging (Figure S5), the Li–O$_2$ battery of MoS$_2$/MoN@CC was still capable of maintaining a stable operation for 64 cycles (640 h), whereas those of MoS$_2$@CC and MoN@CC failed rapidly after only 10 and 6 cycles, respectively (Figure S6). Thus, it becomes evident that the heterostructure composed of MoS$_2$ and MoN can synergisti-

cally enhance the Li–O$_2$ battery performance through lowering the charge/discharge polarization, improving the rate capability, and extending the cycle life. It is worthy to note that MoS$_2$/MoN@CC as the freestanding Li–O$_2$ battery cathode is comparable and even superior to many state-of-the-art oxygen cathodes reported in literature (Table S1).

Since MoN@CC was barely active in catalyzing the reversible oxygen conversion in Li–O$_2$ battery, we then focused on characterizing the morphology and crystal phase of the discharge product-Li$_2$O$_2$ on MoS$_2$/MoN@CC and MoS$_2$@CC in order to seek insights into the heterostructure-mediated reaction mechanism. Figure 4(a) shows the SEM images taken on MoS$_2$/MoN@CC at different discharging and charging depth with a current density of 0.1 mAcm^{-2}. When the discharging capacity was increased from 0.2 to 0.5 and further to 1.0 mAhcm^{-2}, a uniform layer of the discharge product was cumulatively developed on the cathode surface, wrapping around the protruded petals (Figure 4a-I, II and III). Meanwhile, XRD showed that both the MoS$_2$ and MoN signals presented initially on the pristine cathode were diminished after discharg-
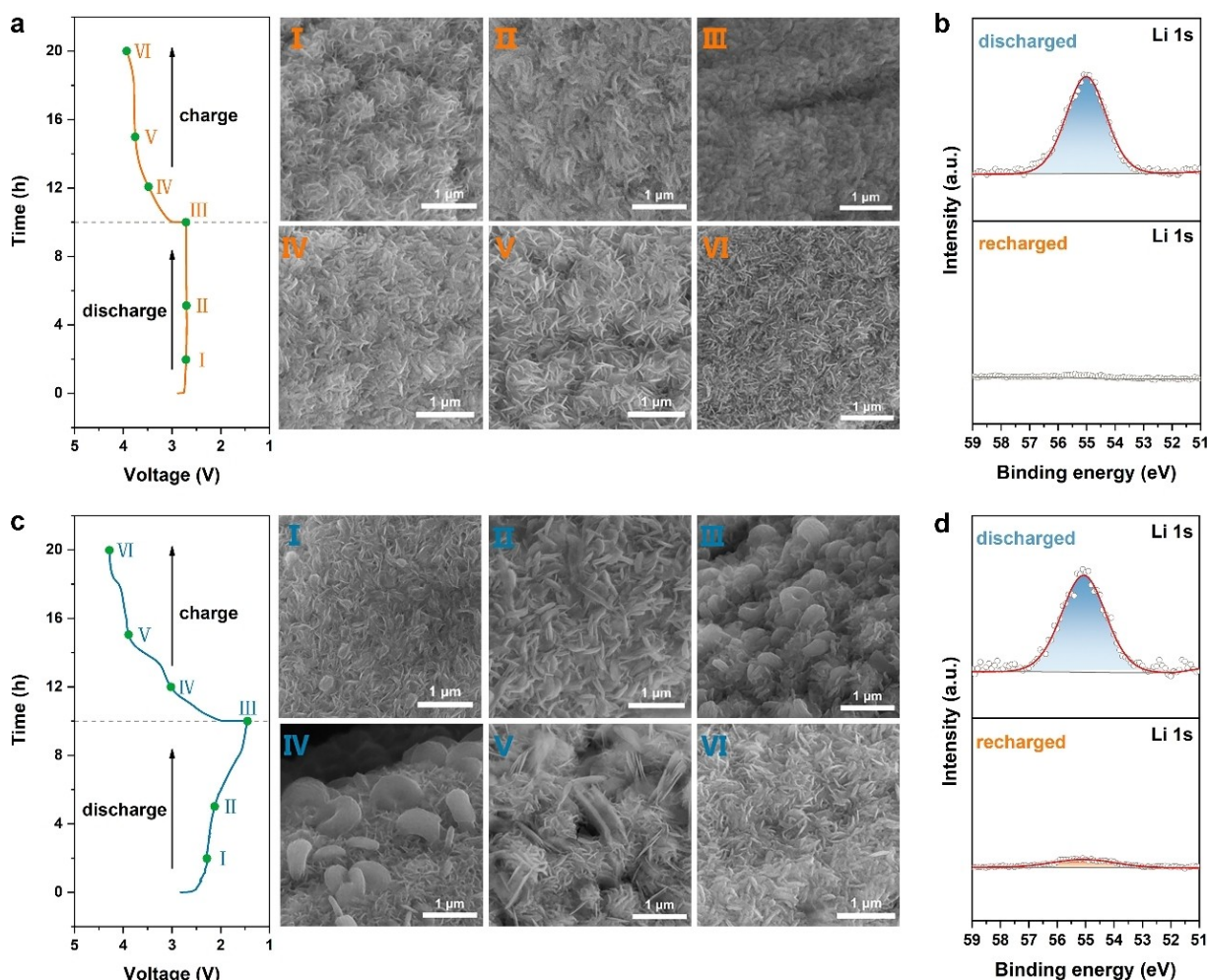

Figure 4. Ex-situ SEM and XPS analyses to monitor the morphology and reversibility of the discharge products. a) SEM images taken on MoS$_2$/MoN@CC at different depth of discharge/charge from I to VI. b) XPS spectra of Li 1s taken on MoS$_2$/MoN@CC at the fully discharged (III) and recharged (VI) states. c) SEM images taken on MoS$_2$@CC at different depth of discharge/charge from I to VI. d) XPS spectra of Li 1s taken on MoS$_2$@CC at the fully discharged (III) and recharged (VI) states.

Batteries & Supercaps

Research Article
doi.org/10.1002/batt.202200222

Chemistry Europe
European Chemical
Societies Publishing

ing to 1.0 mAh cm^{-2}, and failed to identify any crystalline Li_2O_2 phase (Figure 5a).[37] This indicates the discharge products were thick and amorphous, echoing the SEM image shown in Figure 4(a-III) as well as TEM image and selected area electron diffraction (SAED) shown in Figure S7 (a and b). Furthermore, XPS taken on the discharged cathode revealed a prominent Li 1s peak at 55.0 eV (Figure 4b), suggesting that the amorphous discharge product comprises Li_2O_2.[14,38] Upon recharging, the morphology of $MoS_2/MoN@CC$ gradually reverted to its initial state where no visible deposits can be found (Figure 4a-IV, V and VI). Both the XRD peaks of MoS_2 and MoN reemerged after recharging to 1.0 mAh cm^{-2} (Figure 5a), accompanied by the disappearance of Li 1s peak in XPS (Figure 4b).

To further confirm the amorphous discharge product observed on $MoS_2/MoN@CC$ was indeed Li_2O_2, differential electrochemical mass spectroscopy (DEMS) was taken to quantify the electron transfer number of the redox reaction. According to the stoichiometry of $2Li^+ + O_2 + 2e^- \leftrightarrow Li_2O_2$, the consumption/evolution of one O_2 molecule should theoretically involve two electrons. Thus, if the main discharge product was Li_2O_2 rather than LiO_2, Li_2CO_3 and other side products, the measured electron to O_2 ratio (e^-/O_2) should be close to 2.[39,40] As shown by the DEMS spectra in Figure 5(c and d), the calculated e^-/O_2 ratios during discharge and charge were 2.06 and 2.1, respectively. This testified that not only the discharge product on $MoS_2/MoN@CC$ was majorly Li_2O_2, but also its formation/decomposition was reversible.

In a stark contrast, the scenario on $MoS_2@CC$ was drastically different. Immediately upon discharging, granular discharge products began to emerge on the cathode surface (Figure 4c-I), and gradually developed into flaky (Figure 4c-II) and toroidal (Figure 4c-III) shapes. The toroidal discharge product of Li_2O_2
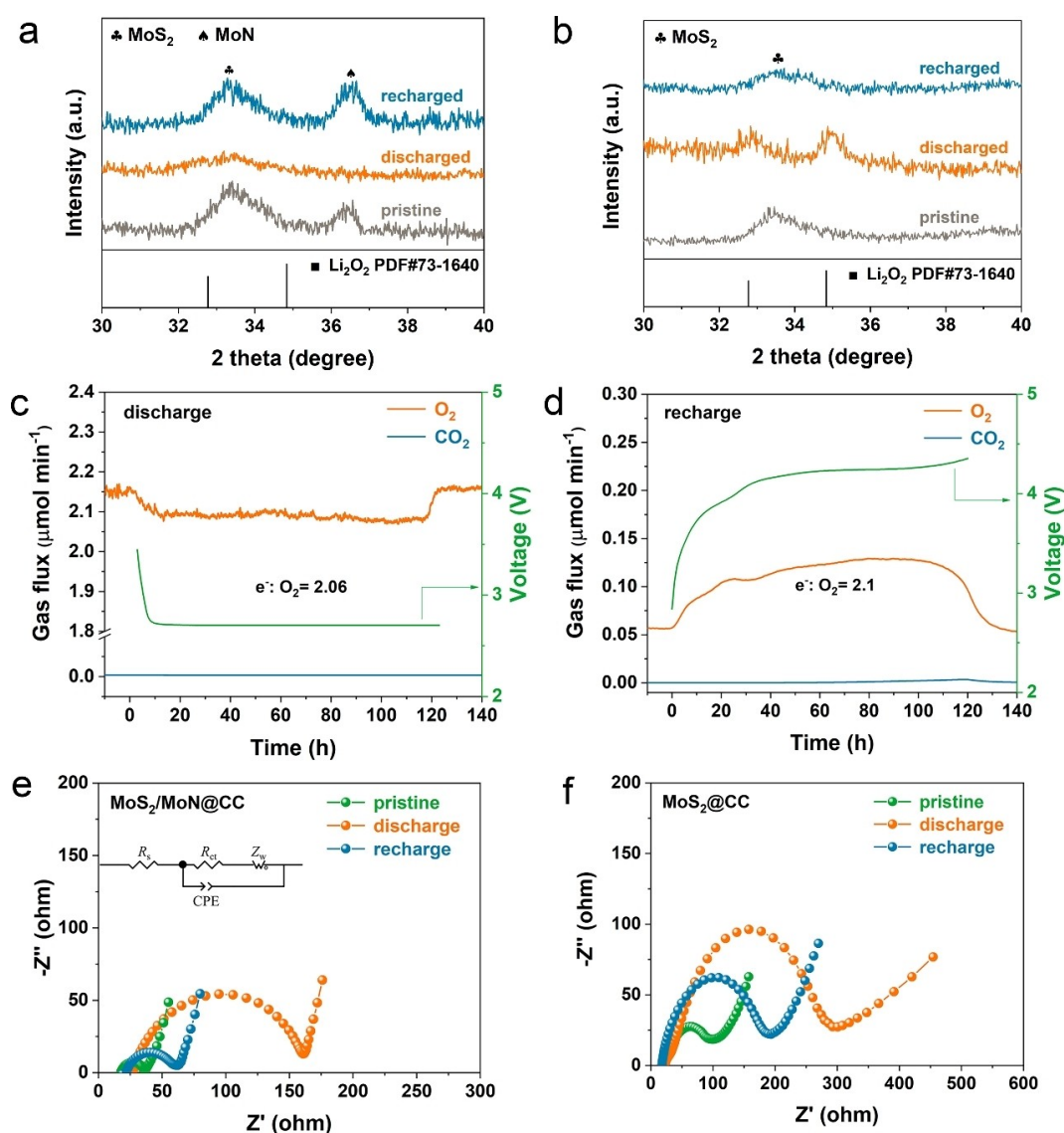
Figure 5. Mechanistic investigations into the heterostructure-mediated charge/discharge processes. a, b) XRD patterns taken on the pristine, discharged, and recharged (a) $MoS_2/MoN@CC$ and (b) $MoS_2@CC$ cathodes. c, d) DEMS spectra collected during the first (c) discharge and (d) charge cycle from the Li–O_2 battery of $MoS_2/MoN@CC$. e, f) EIS spectra taken at different discharge/charge stages on the Li–O_2 batteries of (e) $MoS_2/MoN@CC$ and (f) $MoS_2@CC$.

has been well documented in literature owing to a solvation-mediated solution crystallization process.[8,41] The observed morphological evolution was highly reversible during recharging, with the discharge product reverting from toroids to flakes (Figure 4c-IV, V). Unlike the amorphous Li_2O_2 observed on $MoS_2/MoN@CC$, XRD revealed distinct Li_2O_2 peaks on $MoS_2@CC$ (Figure 5b) owing to the crystalline nature of the toroids, which was in accordance with the results of TEM and SAED (Figure S7c,d). It is worth noting that the crystalline Li_2O_2 (55.1 eV) deposited on $MoS_2@CC$ cathodes surface has higher binding energy than that of amorphous Li_2O_2 (55.0 eV) on $MoS_2/MoN@CC$ cathodes, indicating that the crystalline Li_2O_2 is more difficult to decompose. When the battery was fully recharged, SEM image in Figure 4c-VI shows the discharge products on the cathode were mostly gone, in resonance with the vanishing of Li 1s peak in XPS (Figure 4d) and Li_2O_2 signals in XRD (Figure 5b).[13]

Electrochemical impedance spectroscopy (EIS), however, unveiled more sluggish charge kinetics and less reversible Li_2O_2 decomposition on $MoS_2@CC$ when compared to $MoS_2/MoN@CC$. All the acquired Nyquist plots were fitted to the analogue circuit shown in the inset of Figure 5(e), comprising the serial ohmic resistance (R_s), charge transfer resistance (R_{ct}), Warburg impedance (Z_w), as well as a constant phase element (CPE).[42,43] In the pristine state, the cathode of $MoS_2/MoN@CC$ presented a charge transfer resistance (R_{ct}) value of 18.8 Ω, which increased to 139.2 Ω after discharge and returned to 39.8 Ω after recharge. In comparison, the R_{ct} value of the pristine $MoS_2@CC$ cathode was 87.8 Ω, which is more than four times higher than that of $MoS_2/MoN@CC$, attesting that MoN can significantly enhance the charge kinetics. In addition, both the R_{ct} values of $MoS_2@CC$ after discharge (289.1 Ω) and recharge (172.5 Ω) were drastically higher than those of $MoS_2/MoN@CC$, implying that the crystalline Li_2O_2 is less electrochemically active and reversible. All the Warburg slopes of $MoS_2/MoN@CC$ were notably higher than those of $MoS_2/MoN@CC$, corroborating that the kinetics of Li^+ diffusion in the amorphous Li_2O_2 phase is faster. Collectively, the much enhanced charge kinetics witnessed on $MoS_2/MoN@CC$ well rationalizes the lowered charge/discharge polarization and improved rate capability in $Li-O_2$ batteries, as well as the advantage of amorphous Li_2O_2 in affording reversible deposition/decomposition.
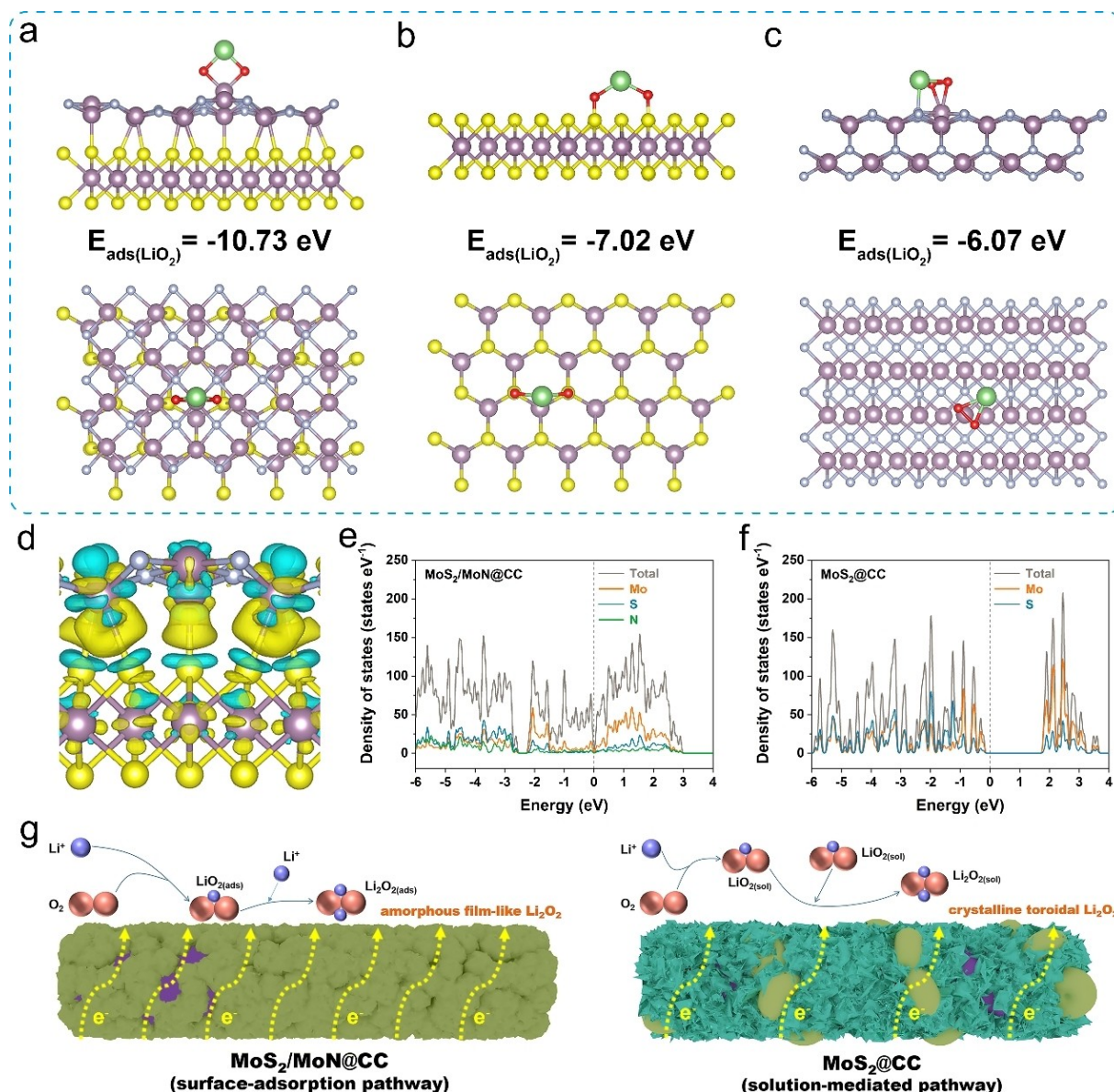
Clearly, our elaborative experimental study above shows that the main difference between $MoS_2/MoN@CC$ and $MoS_2@CC$ in catalyzing Li_2O_2 deposition lies in the modulation of the crystallization process. The $MoS_2@CC$ cathode mainly induces the crystalline form of Li_2O_2 through the solvation-mediated pathway, which is more thermodynamically driven, whereas the deposition of amorphous Li_2O_2 layer on $MoS_2/MoN@CC$ follows a surface growth mechanism that is kinetically preferential. Prior density functional theory (DFT) calculations suggested that amorphous Li_2O_2 is ionically and electronically more conductive than its crystalline form,[44,45] and thus the membranous discharge product covering the whole electrode surface favors the full exploitation of catalytic sites toward reversible ORR/OER. We surmise that the higher conductivity

afforded by MoN and the stronger adsorption of the LiO_2 intermediate (formed through the one-electron reaction $O_2 + e^- + Li^+ \rightarrow LiO_2$) at the heterostructure interface might be the reasons behind the scene, which will be further scrutinized below via DFT simulations.

From our experimental observations, it is most likely that the outmost layer of MoS_2 was partially converted to MoN during the nitridation process, and thus our DFT model is composed of a top MoN layer laid over the MoS_2 substrate (Figures S8–S10). Previous studies have shown that the nucleation and growth of Li_2O_2 are largely governed by the solvation of the LiO_2 intermediate in competition with its surface absorption on the catalytic scaffolds,[46] which is closely related to the Gutmann donor number of the electrolyte and the adsorption energy (ΔE_{ads}) of LiO_2.[47,48] As shown in Figure 6(a–c), the $MoS_2(002)/MoN(200)$ heterostructure manifests a stronger LiO_2 binding energy ($\Delta E_{ads} = -10.73$ eV) than the single-component MoS_2 ($\Delta E_{ads} = -7.02$ eV) and MoN ($\Delta E_{ads} = -6.07$ eV), supporting the preferential binding of the LiO_2 intermediate on the heterostructure, followed by the subsequent surface growth of Li_2O_2. This is mainly due to the electron-pulling effect from MoS_2 on MoN after the two components are brought into intimate contact, as witnessed by the calculated differential charge density profile of the MoS_2/MoN heterostructure shown in Figure 6(d). Specifically, an electron-rich zone was formed at the heterostructure interface due to the delocalization of Mo 3d electrons from MoN in overlap with the S 2p orbitals from MoS_2.[49,50] As a result, the Mo atoms in MoN are positively biased and bond to the oxygens of LiO_2 more strongly. Figure 6(e and f) display the calculated density of states (DOS) for the MoS_2/MoN heterostructure and single-component MoS_2, respectively, with that of the single-component MoN given in Figure S11. While MoS_2 shows a prominent semi-conductive attribute of 1.83 eV in band gap, the heterostructure manifests the metallic nature with the Fermi level residing in the dispersive conduction band. Taken together, both the enhanced LiO_2 adsorption and electric conductivity on the heterostructure support the kinetically driven surface growth of amorphous Li_2O_2 as the discharge product.

Collectively from the above experimental and theoretical evidence, we come up with an overall picture of Li_2O_2 growth on $MoS_2/MoN@CC$ and $MoS_2@CC$, respectively, as depicted in Figure 6(g). Since the $MoS_2/MoN@CC$ possesses a higher electric conductivity and the LiO_2 intermediate adsorption at the heterostructure interface is stronger, the formation of Li_2O_2 mainly follows a kinetics-driven surface growth mechanism through the reaction: $LiO_2 + e^- + Li^+ \rightarrow Li_2O_2$.[1,5] On the other hand, the LiO_2 intermediate manifests a lower binding energy on pristine MoS_2, and therefore is more readily solvated in the electrolyte. Furthermore, due to the poor conductivity of MoS_2, the growth of Li_2O_2 through the disproportionation reaction ($2LiO_{2(sol)} \rightarrow Li_2O_2 + O_2$) tends to occur in the solution phase and is more thermodynamically driven,[1,5] resulting in the toroidal discharge product with high crystallinity.

The different Li_2O_2 morphology observed on $MoS_2/MoN@CC$ and $MoS_2@CC$ further explains the difference in charging

Batteries & Supercaps

Research Article
doi.org/10.1002/batt.202200222

Chemistry
Europe
European Chemical
Societies Publishing

Figure 6. DFT calculations and proposed Li_2O_2 pathways on $MoS_2/MoN@CC$ and $MoS_2@CC$. (a–c) The configuration of LiO_2 binding on (a) $MoS_2(002)/MoN(200)$, (b) $MoS_2(002)$ and (c) MoN(200). d) The differential charge density profile at the $MoS_2(002)/MoN(200)$ interface. e,f) Calculated DOS for (e) the MoS_2/MoN heterostructure and (f) the single-component MoS_2. g) Schematic illustration of the kinetically driven Li_2O_2 growth on $MoS_2/MoN@CC$ following the LiO_2 surface-absorption pathway (left) and the thermodynamically driven Li_2O_2 growth on $MoS_2@CC$ following the LiO_2 solvation-mediated pathway (right).

profiles observed previously in Figure 3(b) (as well as in Figure 4), in which the smoothly ascending curve of $MoS_2/MoN@CC$ correlates to the decomposition of uniform Li_2O_2 layer on surface, and the staircased charging curve of $MoS_2@CC$ correlates to the toroidal Li_2O_2 decomposition. Previous studies have shown the morphology and crystalline structure of Li_2O_2 are highly correlated to the charging overpotential due to limitations in the mass and charge transport.[51–53] In the initial charging phase of the Li–O_2 battery, conformal Li_2O_2 films in good contact with the catalytic sites can be readily decomposed at low voltages. With the increase of the charging capacity, the Li_2O_2 in sufficient contact with the catalytic sites were completely decomposed, and then the leaving bulky Li_2O_2 disintegrate via a sluggish solid-solution reaction due to the

lack of catalyst participation, resulting in moderately high potential was needed to decompose Li_2O_2 to decompose Li_2O_2. So, the end result is that the charge potential increases with the increase of the charging capacity. For $MoS_2/MoN@CC$, conformal Li_2O_2 films in good contact with the catalytic sites can be readily decomposed at low voltages, whereas the bulky Li_2O_2 crystals on $MoS_2@CC$ disintegrate via a sluggish solid-solution reaction that lacks catalyst participation, with substantial charge transfer occurring only at moderately high potentials.[54] As such, the conformal and amorphous discharge product of Li_2O_2 on $MoS_2/MoN@CC$ is favorable to not only avoid parasitic side reactions during charging, but also promote the round-trip energy efficiency by mitigating cell polarization. What's more, the low overpotential in Li–O_2 battery of MoS_2/

Batteries & Supercaps

Research Article
doi.org/10.1002/batt.202200222

Chemistry Europe
European Chemical
Societies Publishing

MoN@CC can be also attributed to the superior catalytic capability of 2D layer-structured MoS_2 with exposed (002) facets.[55–57]

Lastly, the applicability of the freestanding and flexible MoS_2/MoN@CC cathode in deformable Li–O_2 pouch cells was demonstrated by coupling with a lithium foil. Figure 7(a–d) illustrate the as-fabricated pouch cell capable of continuously lighting an LED bulb of 1.8 V input at the flat, folded, twisted, and re-flattened states, endorsing its superb mechanical deformability and durability. At the discharging current density of 0.05 mA cm^{-2}, the pouch cell delivered a total discharge capacity of 24.61 mWh cm^{-2} with a prolonged discharge voltage of 2.69 V (Figure 7e). More impressively, the pouch cell demonstrated a remarkable operational lifetime in the prolonged galvanostatic cycling test at 0.05 mA cm^{-2} with a cut-off capacity of 0.1 mAh cm^{-2}, lasting for over 560 hours with a terminal voltage output of 2.55 V and round-trip efficiency of 57% retained at the end of the test (Figures 7f and S12). As a result, the electrochemical and mechanical superiority of the freestanding MoS_2/MoN@CC cathode demonstrated above should pave the way for their prospective applications in portable power sources and wearable electronics.

Conclusion

In the current study, a facile method was developed to construct the MoS_2/MoN heterostructure on carbon cloth by partially nitridizing the hydrothermally grown MoS_2 layer. The as-fabricated MoS_2/MoN@CC composite, when utilized as the freestanding and binder-free oxygen cathode in Li–O_2 batteries, demonstrated a low charge/discharge polarization of 0.79 V, a high specific capacity of 9.04 mAh cm^{-2}, and a prolonged cycling stability over 200 cycles (800 h) at 0.1 mA cm^{-2}. More importantly, the superb electrochemical performance of MoS_2/MoN@CC, when compared to MoS_2@CC, can be unequivocally attributed to the formation of a preferential amorphous Li_2O_2 layer on the cathode surface, in contrast to the toroidal discharge product of the latter. Further electrochemical and DFT analyses suggest that the higher electric conductivity of MoN and stronger LiO_2 intermediate adsorption on the heterostructure synergistically contribute to the kinetically driven surface growth of Li_2O_2. Consequently, this work sheds new light on modulating the morphology of discharge products by constructing heterostructure interfaces to bolster the performance of Li–O_2 batteries.

Experimental Section

Preparation of MoS_2@CC

Carbon cloth (CC) was first pretreated with HNO_3, followed by the hydrothermal growth of MoS_2 at the CC surfaces. In a typical synthesis procedure, 0.185 g Na_2MoO_4·$2H_2O$ and 0.285 g CH_4N_2S were dissolved in 45 mL distilled water with continuous stirring for 30 mins. The solution immersed with the CC pieces was then transferred into a 100 mL Teflon-lined autoclave and heated at 200 °C for 20 h. After the hydrothermal process, the samples of
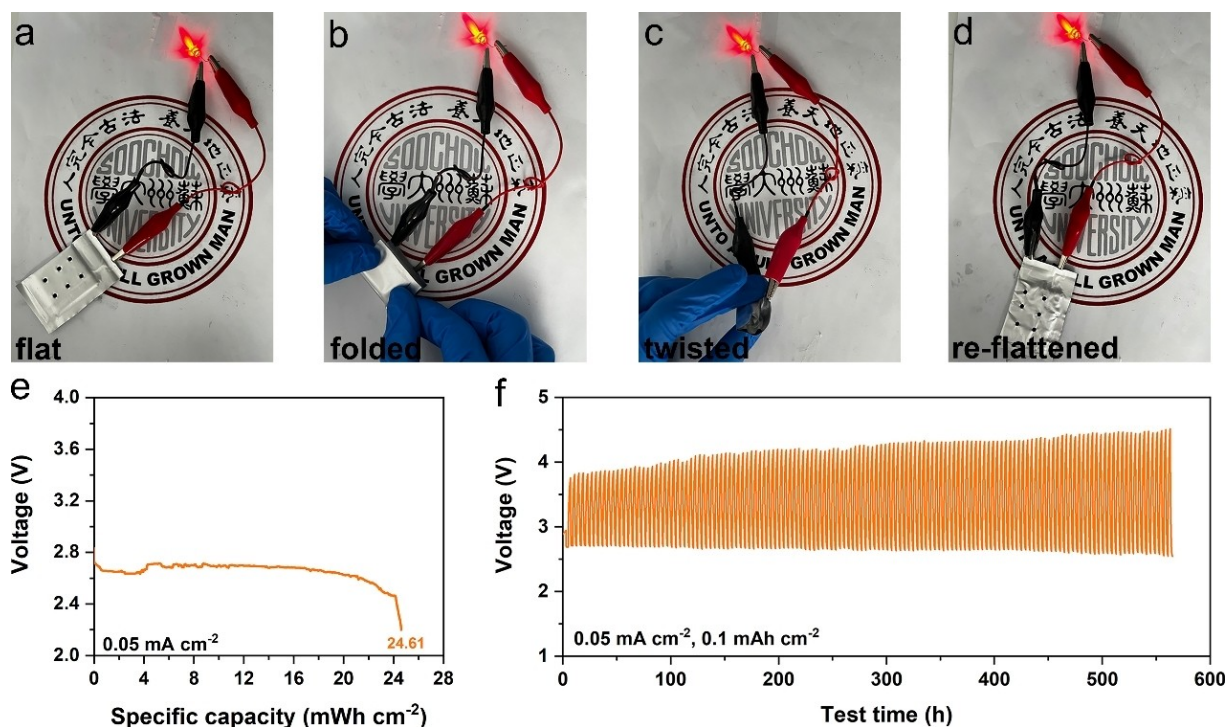
Figure 7. Demonstration of flexible Li–O_2 batteries with high durability. a–d) Photographs showing a flexible Li–O_2 pouch cell to light an LED at different deformation status. e) The full discharge profile of the MoS_2/MoN@CC pouch cell at 0.05 mA cm^{-2} with a cut-off voltage of 2.2 V. f) Galvanostatic cycling performance of the pouch cell at 0.05 mA cm^{-2} with a fixed cycling capacity of 0.1 mAh cm^{-2}.

Batteries & Supercaps

Research Article
doi.org/10.1002/batt.202200222

Chemistry Europe
European Chemical
Societies Publishing

MoS_2@CC were washed with distilled water and dried overnight. The areal mass loading of catalyst on MoS_2@CC is 1.36 mg cm^{-2}.

Preparation of MoS_2/MoN@CC and MoN@CC

For the synthesis of MoS_2/MoN@CC, samples of MoS_2@CC were placed into the CVD furnace. Then, the furnace was heated up to 800 °C and held for 1 h under the mixed gas atmosphere of Ar:NH$_3$=5:1. The synthesis of MoN@CC followed a similar process with the extended nitridation time of 4 h. The areal mass loading of catalyst on MoS_2/MoN@CC and MoN@CC are 1.05 mg cm^{-2} and 0.93 mg cm^{-2}, respectively.

Material characterization

The sample morphology and microstructure were examined by field-emission scanning electron microscopy (SEM) (Hitachi SU8010) and transmission electron microscopy (Thermo Fisher Talos F200X). The crystalline structure was analyzed by powder X-ray diffraction (XRD, Bruker D8 ADVANCE diffractometer equipped with a Cu K_α radiation source). The surface elemental compositions and chemical states were probed by X-ray photoelectron spectroscopy (XPS) (Thermo Fisher, ESCALAB 250Xi) equipped with a monochromated Al K_α source.

Electrochemical measurements

MoS_2/MoN@CC, MoS_2@CC and MoN@CC were used as the free-standing and binder-free cathodes without further treatments. Li foil of 1 mm was used as anode without other treatments. The 2032-type coin cells were assembled in an Ar-filled glove box with both the contents of H_2O and O_2 maintained below 0.1 ppm. The electrolyte employed was 1.0 M LiTFSI in TETRAGLYME without any additives. A fixed amount of electrolyte of 160 µL was used for each cell, and the glass fiber disk with a diameter of 19 mm (Whatman GF/D) was employed as the separator. Galvanostatic charge/discharge measurements were monitored using a LAND CT2001A battery testing system. Electrochemical impedance spectrometry (EIS) measurements within a frequency range from 100 kHz to 0.01 Hz at an amplitude of 5 mV were performed by using the Zahner Zennium-E electrochemical workstation. Cyclic voltammetry (CV) measurements were carried out at a scan rate of 0.5 mV s^{-1} on a CHI760E electrochemical workstation. A quadrupole mass spectrometer (PrismaPlus QME220) with a leak inlet was connected to a customized Swagelok cell assembly for differential electrochemical mass spectrometry (DEMS). All electrochemical measurements were carried out at room temperature.

Computational Details

The Vienna Ab Initio Package (VASP) was used to perform all the density functional theory (DFT) calculations within the generalized gradient approximation (GGA) via Perdew–Burke–Ernzerh (PBE) formulation. The projected augmented wave (PAW) potentials was chosen to describe the ionic cores and valence electrons were taken into account using a plane wave basis set with a kinetic energy cut-off of 400 eV. Partial occupancies of the Kohn–Sham orbitals were allowed using the Gaussian smearing method and a width of 0.05 eV. The electronic energy was considered self-consistent when the energy change was smaller than 10^{-5} eV. A geometry optimization was considered convergent when the force change was smaller than 0.02 eV/Å. Grimme's DFT-D3 methodology was used to describe the dispersion interactions.

The equilibrium lattice constants of hexagonal MoS_2 unit cell were optimized, when using a 13×13×3 Monkhorst-Pack k-point grid for Brillouin zone sampling, to be a=3.165 Å, c=12.352 Å. We then use it to construct a rectangular MoS_2(002) surface model (Figure S7) with p(5×2$\sqrt{3}$) periodicity in the x and y directions and one stoichiometric layer in the z direction separated by a vacuum layer in the depth of 15 Å in order to separate the surface slab from its periodic duplicates. This surface model contains 20 Mo and 40 S atoms. During structural optimizations, the gamma point in the Brillouin zone was used for k-point sampling, and all atoms were allowed to relax.

The equilibrium lattice constant of cubic MoN unit cell was optimized, when using a 9×9×9 Monkhorst-Pack k-point grid for Brillouin zone sampling, to be a=4.312 Å. We then use it to construct a rectangular MoN(200) surface model (Figure S8) with p(3×2) periodicity in the x and y directions and two stoichiometric layers in the z direction separated by a vacuum layer in the depth of 15 Å in order to separate the surface slab from its periodic duplicates. This surface model contains 48 Mo and 48 N atoms. During structural optimizations, the gamma point in the Brillouin zone was used for k-point sampling, and the bottom stoichiometric layer was fixed while the top one was allowed to relax.

For the MoS_2(002)/MoN(200) heterojunction surface model, one MoN(200) stoichiometric layer was placed onto the above MoS_2(002) model. During structural optimizations, the gamma point in the Brillouin zone was used for k-point sampling, and the MoS_2 part was fixed while the MoN part was allowed to relax.

The adsorption energy (E_{ads}) of adsorbate A was defined as:

$$E_{ads} = E_{A/surf} - E_{surf} - E_{A(g)}$$

where $E_{A/surf}$, E_{surf} and $E_{A(g)}$ are the energy of adsorbate A adsorbed on the surface, the energy of clean surface, and the energy of isolated A molecule in a cubic periodic box with a side length of 20 Å and a 1×1×1 Monkhorst-Pack k-point grid for Brillouin zone sampling, respectively.

Acknowledgements

Conflict of Interest

The authors declare no conflict of interest.

Data Availability Statement

The data that support the findings of this study are available from the corresponding author upon reasonable request.

[1] W. J. Kwak, R. D. Sharon, C. Xia, H. Kim, L. R. Johnson, P. G. Bruce, L. F. Nazar, Y. K. Sun, A. A. Frimer, M. Noked, S. A. Freunberger, D. Aurbach, *Chem. Rev.* **2020**, *120*, 6626–6683.

[2] D. Aurbach, B. D. McCloskey, L. F. Nazar, P. G. Bruce, *Nat. Energy* **2016**, *1*, 1–11.

[3] A. Jaradat, C. Zhang, S. K. Singh, J. Ahmed, A. Ahmadiparidari, L. Majidi, S. Rastegar, Z. Hemmat, S. Wang, A. T. Ngo, *Small* **2021**, *17*, 2102072.

[4] Z. Chang, J. Xu, X. Zhang, *Adv. Energy Mater.* **2017**, *7*, 1700875.

[5] T. Liu, J. P. Vivek, E. W. Zhao, J. Lei, N. Garcia-Araez, C. P. Grey, *Chem. Rev.* **2020**, *120*, 6558–6625.

[6] H.-D. Lim, B. Lee, Y. Bae, H. Park, Y. Ko, H. Kim, J. Kim, K. Kang, *Chem. Soc. Rev.* **2017**, *46*, 2873–2888.

[7] L. Liu, Y. Liu, C. Wang, X. Peng, W. Fang, Y. Hou, J. Wang, J. Ye, Y. Wu, *Small Methods* **2022**, *6*, 2101280.

[8] R. R. Mitchell, B. M. Gallant, Y. Shao-Horn, C. V. Thompson, *J. Phys. Chem. Lett.* **2013**, *4*, 1060–1064.

[9] J. Huang, B. Zhang, Z. Bai, R. Guo, Z. L. Xu, Z. Sadighi, L. Qin, T. Y. Zhang, G. Chen, B. Huang, J. K. Kim, *Adv. Funct. Mater.* **2016**, *26*, 8290–8299.

[10] L. Johnson, C. Li, Z. Liu, Y. Chen, S. A. Freunberger, P. C. Ashok, B. B. Praveen, K. Dholakia, J. M. Tarascon, P. G. Bruce, *Nat. Chem.* **2014**, *6*, 1091–1099.

[11] A. Hu, W. Lv, T. Lei, W. Chen, Y. Hu, C. Shu, X. Wang, L. Xue, J. Huang, X. Du, H. Wang, K. Tang, C. Gong, J. Zhu, W. He, J. Long, J. Xiong, *ACS Nano* **2020**, *14*, 3490–3499.

[12] X. Gao, Y. Chen, L. Johnson, P. G. Bruce, *Nat. Mater.* **2016**, *15*, 882–888.

[13] R. A. Wong, A. Dutta, C. Yang, K. Yamanaka, T. Ohta, A. Nakao, K. Waki, H. R. Byon, *Chem. Mater.* **2016**, *28*, 8006–8015.

[14] F. Li, M. L. Li, H. F. Wang, X. X. Wang, L. J. Zheng, D. H. Guan, L. M. Chang, J. J. Xu, Y. Wang, *Adv. Mater.* **2022**, *34*, 2107826.

[15] E. Yilmaz, C. Yogi, K. Yamanaka, T. Ohta, H. R. Byon, *Nano Lett.* **2013**, *13*, 4679–4684.

[16] M. Asadi, B. Kumar, C. Liu, P. Phillips, P. Yasaei, A. Behranginia, P. Zapol, R. F. Klie, L. A. Curtiss, A. Salehi-Khojin, *ACS Nano* **2016**, *10*, 2167–2175.

[17] B. He, G. Li, J. Li, J. Wang, H. Tong, Y. Fan, W. Wang, S. Sun, F. Dang, *Adv. Energy Mater.* **2021**, *11*, 2003263.

[18] X. Zheng, X. Han, Y. Cao, Y. Zhang, D. Nordlund, J. Wang, S. Chou, H. Liu, L. Li, C. Zhong, *Adv. Mater.* **2020**, *32*, 2000607.

[19] Q. Xia, L. Zhao, D. Li, J. Wang, L. Liu, C. Hou, X. Liu, H. Xu, F. Dang, J. Zhang, *J. Mater. Chem. A* **2021**, *9*, 19922–19931.

[20] Z. Hou, C. Shu, R. Zheng, C. Liu, Z. Ran, T. Yang, P. Hei, Q. Zhang, J. Long, *J. Mater. Chem. A* **2020**, *8*, 16636–16648.

[21] Q. Xia, D. Li, L. Zhao, J. Wang, Y. Long, X. Han, Z. Zhou, Y. Liu, Y. Zhang, Y. Li, A. A. A. Adam, S. Chou, *Chem. Sci.* **2022**, *13*, 2841–2856.

[22] S. Huang, Z. Wang, Y. Von Lim, Y. Wang, Y. Li, D. Zhang, H. Y. Yang, *Adv. Energy Mater.* **2021**, *11*, 2003689.

[23] B. Qian, Y. Zhang, X. Hou, D. Bu, K. Zhang, Y. Lan, Y. Li, S. Li, T. Ma, X. M. Song, *Small* **2022**, *18*, 2103933.

[24] P. Wang, C. Li, S. Dong, X. Ge, P. Zhang, X. Miao, R. Wang, Z. Zhang, L. Yin, *Adv. Energy Mater.* **2019**, *9*, 1900788.

[25] M. Li, X. Wang, F. Li, L. Zheng, J. Xu, J. Yu, *Adv. Mater.* **2020**, *32*, 1907098.

[26] D. Li, L. Zhao, Q. Xia, L. Liu, W. Fang, Y. Liu, Z. Zhou, Y. Long, X. Han, Y. Zhang, J. Wang, Y. Wu, H. Liu, *Small* **2022**, *18*, 2105752.

[27] Q. Xia, L. Zhao, Z. Zhang, J. Wang, D. Li, X. Han, Z. Zhou, Y. Long, F. Dang, Y. Zhang, S. Chou, *Adv. Sci.* **2021**, *8*, 2103302.

[28] Y. Yan, Z. Ran, T. Zeng, X. Wen, H. Xu, R. Li, C. Zhao, C. Shu, *Small* **2022**, *18*, 2106707.

[29] S. Wang, S. Feng, J. Liang, Q. Su, F. Zhao, H. Song, M. Zheng, Q. Sun, Z. Song, X. Jia, J. Yang, Y. Li, J. Liao, R. Li, X. Sun, *Adv. Energy Mater.* **2021**, *11*, 2003314.

[30] A. Hu, C. Shu, X. Qiu, M. Li, R. Zheng, J. Long, *ACS Sustainable Chem. Eng.* **2019**, *7*, 6929–6938.

[31] A. Hu, C. Shu, C. Xu, J. Li, R. Liang, R. Zheng, M. Li, Z. Ran, J. Long, *Chem. Eng. J.* **2020**, *382*, 122854.

[32] A. Wu, Y. Gu, Y. Xie, H. Yan, Y. Jiao, D. Wang, C. Tian, *J. Alloys Compd.* **2021**, *867*, 159066.

[33] S.-C. Wu, Y.-H. Huang, C.-R. Liao, S.-Y. Tang, T.-Y. Yang, Y.-C. Wang, Y.-J. Yu, T.-P. Perng, Y.-L. Chueh, *Nano Energy* **2021**, *90*, 106590.

[34] X. Mu, C. Xia, B. Gao, S. Guo, X. Zhang, J. He, Y. Wang, H. Dong, P. He, H. Zhou, *Energy Storage Mater.* **2021**, *41*, 650–655.

[35] X. Dai, K. Du, Z. Li, H. Sun, Y. Yang, X. Zhang, X. Li, H. Wang, *Chem. Eng. Sci.* **2015**, *134*, 572–580.

[36] G. D. Sun, H. Q. Chang, G. H. Zhang, B. J. Yan, K. C. Chou, *J. Am. Ceram. Soc.* **2019**, *102*, 7178–7186.

[37] L. Wei, Y. Ma, Y. Gu, X. Yuan, Y. He, X. Li, L. Zhao, Y. Peng, Z. Deng, *ACS Appl. Mater. Interfaces* **2021**, *13*, 28295–28303.

[38] Z. Zhu, X. Shi, G. Fan, F. Li, J. Chen, *Angew. Chem.* **2019**, *58*, 19021–19026.

[39] Y. Ma, L. Wei, Y. Gu, J. Hu, Y. Chen, P. Qi, X. Zhao, Y. Peng, Z. Deng, Z. Liu, *Adv. Funct. Mater.* **2020**, *30*, 2007218.

[40] Y. Ma, P. Qi, J. Ma, L. Wei, L. Zhao, J. Cheng, Y. Su, Y. Gu, Y. Lian, Y. Peng, Y. Shen, L. Chen, Z. Deng, Z. Liu, *Adv. Sci.* **2021**, *8*, 2100488.

[41] D. Zhai, H. H. Wang, J. Yang, K. C. Lau, K. Li, K. Amine, L. A. Curtiss, *J. Am. Chem. Soc.* **2013**, *135*, 15364–15372.

[42] Y. Feng, H. Xue, T. Wang, H. Gong, B. Gao, W. Xia, C. Jiang, J. Li, X. Huang, J. He, *ACS Sustainable Chem. Eng.* **2019**, *7*, 5931–5939.

[43] Y. Chen, F. Li, D.-M. Tang, Z. Jian, C. Liu, D. Golberg, A. Yamada, H. Zhou, *J. Mater. Chem. A* **2013**, *1*, 13076–13081.

[44] M. D. Radin, D. J. Siegel, *Energy Environ. Sci.* **2013**, *6*, 2370–2379.

[45] F. Tian, M. D. Radin, D. J. Siegel, *Chem. Mater.* **2014**, *26*, 2952–2959.

[46] C. Shu, C. Wu, J. Long, H. Guo, S.-X. Dou, J. Wang, *Nano Energy* **2019**, *57*, 166–175.

[47] Y. Yao, J. Cao, W. Yin, Q. Zhang, L. Yang, X. Wei, *J. Phys. Chem. C* **2021**, *125*, 4363–4370.

[48] Z. Lyu, Y. Zhou, W. Dai, X. Cui, M. Lai, L. Wang, F. Huo, W. Huang, Z. Hu, W. Chen, *Chem. Soc. Rev.* **2017**, *46*, 6046–6072.

[49] Z. F. Huang, J. Song, K. Li, M. Tahir, Y. T. Wang, L. Pan, L. Wang, X. Zhang, J. J. Zou, *J. Am. Chem. Soc.* **2016**, *138*, 1359–1365.

[50] J. Xie, J. Zhang, S. Li, F. Grote, X. Zhang, H. Zhang, R. Wang, Y. Lei, B. Pan, Y. Xie, *J. Am. Chem. Soc.* **2013**, *135*, 17881–17888.

[51] Y. Li, R. Zhang, B. Chen, N. Wang, J. Sha, L. Ma, D. Zhao, E. Liu, S. Zhu, C. Shi, N. Zhao, *Energy Storage Mater.* **2022**, *44*, 285–295.

[52] S. Ganapathy, B. D. Adams, G. Stenou, M. S. Anastasaki, K. Goubitz, X. F. Miao, L. F. Nazar, M. Wagemaker, *J. Am. Chem. Soc.* **2014**, *136*, 16335–16344.

[53] J. Yang, D. Zhai, H. H. Wang, K. C. Lau, J. A. Schlueter, P. Du, D. J. Myers, Y. K. Sun, L. A. Curtiss, K. Amine, *Phys. Chem. Chem. Phys.* **2013**, *15*, 3764–3771.

[54] Y. Xing, Y. Yang, R. Chen, M. Luo, N. Chen, Y. Ye, J. Qian, L. Li, F. Wu, S. Guo, *Small* **2018**, *14*, 1704366.

[55] G. Zhang, G. Li, J. Wang, H. Tong, J. Wang, Y. Du, S. Sun, F. Dang, *Adv. Energy Mater.* **2022**, *12*.

[56] L. Guo, L. Tan, A. Xu, G. Li, G. Zhang, R. Liu, J. Wang, Y. Du, F. Dang, *Energy Storage Mater.* **2022**, *50*, 96–104.

[57] J. Li, K. Han, J. Huang, G. Li, S. Peng, N. Li, J. Wang, W. Zhang, Y. Du, Y. Fan, W. Wang, F. Dang, *Energy Storage Mater.* **2021**, *35*, 669–678.